Article

A Laboratory and Field Universal Estimation Method for Tire–Pavement Interaction Noise (TPIN) Based on 3D Image Technology

Hui Wang [1,2,*]☉, Xun Zhang [2] and Shengchuan Jiang [3,4]

1   Key Laboratory of New Technology for Construction of Cities in Mountain Area, Chongqing University, Ministry of Education, Chongqing 400045, China
2   School of Civil Engineering, Chongqing University, Chongqing 400045, China
3   The Key Laboratory of Road and Traffic Engineering, Ministry of Education, Tongji University, Shanghai 201804, China
4   Shanghai Tonglu Cloud Transportation Technology Co. Ltd., Shanghai 201800, China
*   Correspondence: mickysophy@cqu.edu.cn; Tel.: +86-18616153020

Abstract: Tire–pavement interaction noise (TPIN) accounts mainly for traffic noise, a sensitive parameter affecting the eco-based maintenance decision outcome. Consistent methods or metrics for lab and field pavement texture evaluation are lacking. TPIN prediction based on pavement structural and material characteristics is not yet available. This paper used 3D point cloud data scanned from specimens and road pavement to conduct correlation and clustering analysis based on representative 3D texture metrics. We conducted an influence analysis to exclude macroscope pavement detection metrics and macro deformation metrics' effects (international roughness index, IRI, and mean profile depth, MPD). The cluster analysis results verified the feasibility of texture metrics for evaluating lab and field pavement wear, differentiating the wear states. TPIN prediction accuracy based on texture indicators was high (R^2 = 0.9958), implying that it is feasible to predict the TPIN level using 3D texture metrics. The effects of pavement texture changes on TPIN can be simulated by laboratory wear.

Keywords: traffic noise; tire–pavement interaction noise (TPIN); texture metrics; clustering; machine-learning-based prediction

1. Introduction

Traffic noise accounts for about 70% of the total environmental noise, and road noise accounts for about 80% of the traffic noise [1]. The noise level was found to be the most sensitive parameter affecting the road management decision outcome, compared to other metrics, through sensitivity analysis [2]. The traffic noise pollution is more severe during the off-peak hours than the rush hours, resulting from the increase in speed and traffic volume of the traffic flow [3]. We should be more concerned about the relative high-speed free-flow situation. The pavement condition index has a negative impact on noise for all types of intersections, and the effect of pavement surface conditions is noticeable once the traffic speed is high [4]. Cao et al. (2020) used a sustainable multiobjective decision support system to maintain the low-noise functionality of porous pavement networks and found that the largest average noise reduction was always accompanied by the highest costs and GHG emissions from the intervention [5]. The measured noise spectra had a similar distribution, and both spectra indicated a significant reduction of noise with microsurfacing application [6]. To better plan road maintenance based on ecological costs, we must find a simple method suitable for laboratory studies and field noise prediction. For properly maintained automobiles and trucks, the tire–pavement intersection noise (TPIN) is the dominant sub-resource of highway traffic noise at speeds above 50 km/h and slightly higher for trucks [7]. When pavement wavelength spectra are transformed into

the frequency domain considering vehicle speed and hearing sensitivity, the contribution of texture to noise becomes apparent. However, data to define quantitative functional relationships are not currently available [8]. The first components of the cepstrum in the frequency band of 3 to 5 kHz have a high correlation with macrotexture, but only a narrow range can be monitored via TPIN sensors [9,10]. Macrotexture profiling has been correlated highly with the acoustic properties of asphalt pavements [11].

For the lab test of TPIN, the tire roll-off (TR) method was developed to quantify the TPIN pressure spectrum at low speeds [12]. However, low speed limits TR's use conditions. A circular specimen holder track facility (called HTP²) was developed to measure TPIN at higher speeds (70 km/h, eventually 100 km/h), and the feasibility of this method was verified based on eight different pavement surface types [13]. The lab types of equipment are expensive, and the equipment's quality may change the tire's vibration characteristics. For the field test, the advantage of the tire/vehicle exterior noise measurements using onboard techniques is that the noise components other than tire noise are basically excluded or can be ignored [14].

A model for predicting TPIN of porous asphalt mixes based on macroscopic texture index was proposed, and the model's validity was verified using TR tests [15]. According to the grey relational analysis, air void content is the most crucial factor affecting the noise reduction performance of asphalt pavements, followed by surface texture [16]. Normal maximum aggregate size, Bailey metrics control texture, and volumetrics can help designers choose the suitable gradation to accomplish the noise target [17]. PPM was found to have greater acoustic absorption capacity than OGFC, especially for tire vibration noise, as measured by BPN and noise meter [18]. A higher air void content and larger nominal aggregate size lead to better sound absorption [19]. However, acoustic absorption cannot be considered a TPIN reduction mechanism in certain types of pavements [20]. Higher pavement texture levels could enhance skid resistance and reduce noise simultaneously at different frequency bands [21]. The simulation results of traffic noise in the laboratory show that A-weighted 1/3 octave OASPL of the intermediate-frequency band (200–1600 Hz) is the highest, while the low-frequency band (20–160 Hz) is the lowest [22]. Above all, most studies on the relationship between texture features and noise are based on lab simulations. However, the texture features of specimens differ significantly from those of the actual pavements [23], limiting the application of the research findings.

TPIN is not just related to macrotexture amplitude (MPD); other pavement characteristics are involved in its generation, and sections with higher MPD values are not the noisiest sections [24]. Loopway CPX-based experiments found that the noise level increases with increasing macrotexture depth and decreases with decreasing porosity of the surface mixture, but both are velocity-dependent [25]. TPIN dominates for passenger vehicles above 40 km/h, and 70 km/h for trucks [26]. The trend of TPIN control might not only focus on reducing the noise level and tuning the spectral shape [27]. The overpressure reached during the contact increases with the volume variation of the cavity and the rolling speed [28]. The FEM-BEM method for predicting sound pressure was satisfactory in demonstrating TPIN trends for different pavement surface characteristics, and the texture level is positively related to TPIN [29]. Based on 64 test sections with 18 mix volume design parameters without texture metrics, the highest R-squared for CPX80 (TPIN detected by CPX at 80 km/h) prediction was only 0.59 [30]. Vehicle type and driving speed are important factors affecting the vehicle noise spectrum [31]. Cao et al. (2020) built ANN and SVM models for CPX noise prediction based on collected data (surface thickness, binder content, maximum aggregate size, air void content, pavement age, and vehicle speed) from 270 asphalt pavement sections in Hong Kong, and it was found that the rate of acoustic change varied over a range rather than remaining a constant value, depending on the pavement age and vehicle speed level [32]. The two-dimensional (fractal) method is most useful in distinguishing freshly laid pavements, but the sensitivity is reduced in moderate-wear classes [33]. There is a lack of consistent methods or metrics that can be used for lab and field pavement texture evaluation or TPIN prediction.

Three-dimensional pavement texture metrics have higher correlation coefficients with TPIN than 2D metrics [21]. A commercial 3D laser scanner can accurately reflect the 3D features of pavement macrotexture by comparing four pavement surfaces of different gradations [34]. The RMSR and the MTD obtained by the close-range photogrammetry system can generally achieve the same accuracy level as the laser measurement method [35]. The results of ITAM correlate well with those of SLP [36], SPM, and HFT [37]. The processed point cloud data could precisely characterize the actual pavement macrotexture [38]. Weng et al. (2022) applied image-based multiscale features for texture depth estimation, and the random forest model yielded the best results (cross-fold validation R^2 = 0.8192) [39]. A 3D model generated by close-range photogrammetry was compared to the model developed by a laser scanner, and the average error was found to be 4.2% [40]. The advantage of the tire/vehicle exterior noise measurements using onboard techniques is that the noise components other than tire noise are excluded or can be ignored [26]. Based on the analysis of the physical mechanisms, it was found that the dominant direction of TPIN is the rear side of the tire (the opposite direction of travel) [14]. Therefore, we chose a microphone sensing device mounted in the opposite direction for TPIN measurement and a close-range 3D camera to collect texture data. Lab and field pavement texture data and typical TPIN on site were obtained to find a feasible method for the TPIN lab and field integration study.

2. Methodology

2.1. The Framework of This Study

Figure 1 shows the framework of our study. Firstly, the point cloud data of pavement texture and mixture specimens were obtained using a close-range 3D camera; secondly, we collected TPIN data on general wear and worn roads at car-free campuses. For subsequent studies, representative 3D texture metrics were selected based on Spearman correlation analysis. Mix specimens of different types and abrasion levels were mixed with the measured pavement texture data to conduct a clustering analysis to confirm the lab and field versatility of indicators. TPIN prediction models based on the texture metrics selected were established to verify the feasibility of the estimation method.
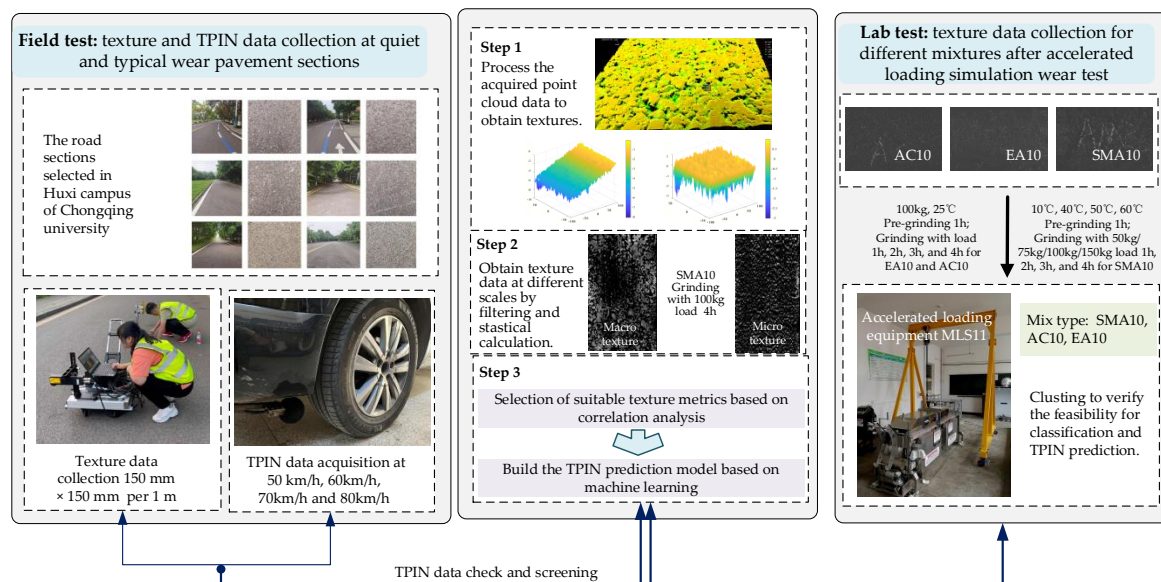

Figure 1. The framework of our study.

2.2. Data Acquisition and Processing

2.2.1. Texture Data Collection

To collect texture data, we used the Gocator high-speed 3D laser contour sensor with a maximum field of view (FOV) of 365 mm and 1280 laser line contour points. For the

field test, the resolution in the x-direction was 0.171 mm, the resolution in the y-direction was 0.116 mm, the resolution in the z-direction was 0.013 mm, and the set motion speed in the y-direction was 50 mm/s. For the lab test, the resolution of laboratory specimens was 0.150–0.181 mm in the x-direction, 0.116–0.188 mm in the y-direction, and 0.0034 mm in the z-direction. The same size of 689 rows and 129 columns were used to calculate the texture metrics.

2.2.2. Texture Data Preprocess Method

After scanning, texture data were preprocessed by data standardization to remove the data with large amounts of missing values at the edges and form a uniform size sample. The effect of road slope on the data was modified by the least squares method according to ISO Standard No. 13473-4 [41]. For missing internal values, the linear interpolation method was used to fill these. The data preprocess method was proven suitable for field [22] and lab [20] data.

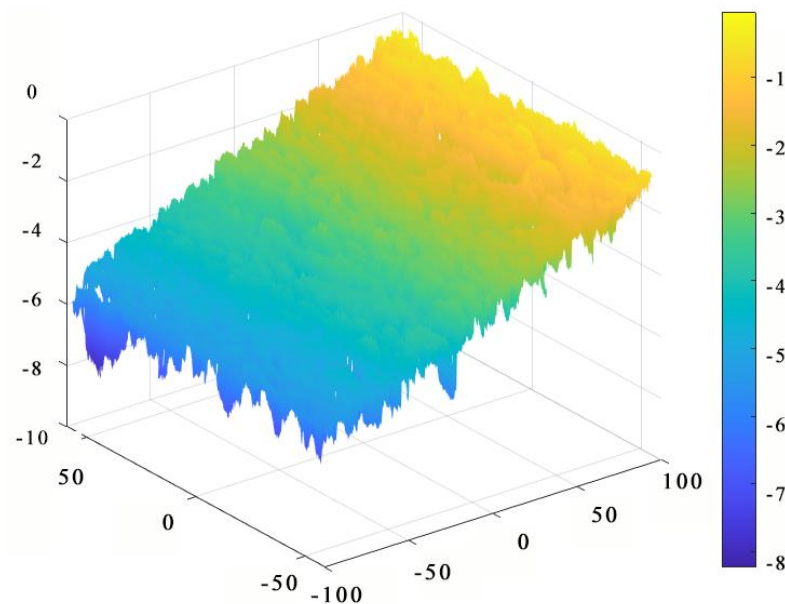The data before and after preprocessing are shown in Figures 2 and 3.

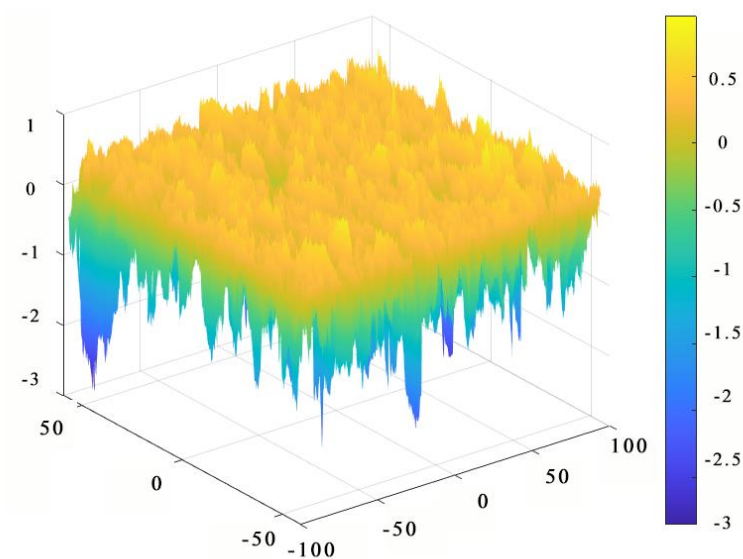
Figure 2. The example of the original detection data.

Figure 3. The example of the data after preprocessing.

2.2.3. Texture Metrics Calculation

The texture data were calculated based on texture separation. Fourteen metrics were chosen, including power spectral density function integration of microtexture (*WT*), power spectral density function integration of macrotexture (*HT*), energy (*ENE*), contrast (*CON*), entropy (*ENT*), ENE of macrotexture (*HENE*), *CON* of macrotexture (*HCON*), ENT of macrotexture (*HENT*), ENE of microtexture (*WENE*), CON of microtexture (*WCON*), ENT of microtexture (*WENT*), fractal dimension (*D*), D of macrotexture (*HD*), and *D* of microtexture (*WD*). The calculation methods were according to our previous study [22].

2.2.4. TPIN Data Collection and Data Representation Analysis

The data collected were the microphone signal voltage values, and the sound pressure was converted to 50 mv/Pa according to the microphone's sensitivity. The noise data of each texture data collection location were calculated by Equation (1):

$$N_i = \frac{v}{0.02} \times i \tag{1}$$

where N_i is the noise corresponding to the texture data at point *i*, *V* is the vehicle speed, 0.02 is the noise acquisition period, and *i* is the texture position of the *i-th* point.

Limited by the distance of the tested section, the acceleration, and the deceleration behaviors during the test, we selected data that were less affected by accelerating and had a more significant gain according to the data characteristics to carry out the TPIN study. The relationship between the instantaneous vehicle speed and TPIN data at the corresponding location was analyzed by box plot. The influences of factors other than texture were determined by relation analysis of IRI, macroscopic profile depth (MPD), and TPIN values.

2.3. Texture Metrics Selection

2.3.1. Texture Metrics Selection by Correlation Analysis

To further reduce the data of texture feature indicators and remove redundant indicators, the correlation analysis of all texture indicators was performed by the Spearman correlation coefficients that applied to data not strictly conforming to the normal distribution. Metrics of additional specimens before and after abrasion of fine-grained asphalt mixes with the same maximum nominal particle size as the field pavements were included.

The Spearman coefficient is a nonparametric measure of the dependence of two variables, which can be calculated by Equation (2):

$$r_s = 1 - \frac{6 \sum d_i^2}{n(n^2 - 1)}, \tag{2}$$

where *n* denotes the number of data, and d_i denotes the difference between the two metrics.

2.3.2. Application Validation of Texture Metrics Based on Clustering

The K-means algorithm [42] calculated the distance between sample points and the cluster center of mass. The sample points close to the cluster center of mass are classified into the same class of clusters. The more distant the two samples are, the less similar they are. Euclidean distance was used in this study, and its calculation formula is as follows (3):

$$\rho = \sqrt{\sum_{i=1}^{6} (x_i - x_{i0})^2} \tag{3}$$

where x_i is the *i-th* metric's value, and x_{i0} is the *i-th* metric's cluster center value.

The internal metrics, including (*CH*), Davies–Bouldin index (*DBI*), and silhouette coefficient (*SC*), were used to carry out the basic unsupervised clustering effect evaluation.

The external metrics, including purity, Rand index (*RI*), and mutual information entropy (*MI*), were used to evaluate the classification effect.

Calinski–Harabasz (*CH*) is obtained from the ratio of separation to tightness. Thereby, a larger *CH* represents a tighter class and a more dispersed class. The calculation method is shown in (4):

$$CH = trBktr(Wk)m - kk - 1CH = \frac{tr(B_k)}{tr(W_k)} \frac{m-k}{k-1} \tag{4}$$

where *tr* is the trace of the matrix, *Bk* is the covariance matrix between categories, *Wk* is the covariance matrix of the data within categories, m is the number of samples in the training set, and k is the number of categories.

DBI measures the ratio of the intracluster distance to the intercluster distance after any two clusters [43]. The smaller the index, the smaller the intracluster distance and the higher the intracluster similarity. The larger the intercluster distance, the lower the intercluster similarity. Its calculation formula is (5).

$$DBI = \frac{1}{n} \sum_{i=1}^{n} max_{(i \neq j)} \left(\frac{S_i + S_j}{M_{ij}} \right) \tag{5}$$

where *n* is the clustering number, S_i is the distance between data in class *i* and cluster centroid, S_j is the distance between data in class *j* and cluster centroid, and M_{ij} is the distance between the cluster centres of class *i* and *j*.

SC is the average of all the sample silhouette coefficients [44]. The range of *SC* is [−1, 1], and the more similar the distance between samples of the same category and the more distant the distance between samples of different categories, the higher the score. Its calculation formula is (6):

$$SC = \frac{1}{n} \sum_{i=1}^{n} \frac{S_i - S_j}{max M_{ij}} \tag{6}$$

RI takes values in the range of [0, 1], and a larger value means that the clustering results match the actual situation, which is calculated by Equation (7) [45].

$$RI = \frac{a+b}{C_n^2} \tag{7}$$

where *a* is the right logarithms of real labels and clustering results of homogeneous elements, *b* is the logarithms of real labels and clustering results of homogeneous elements, and *n* is the total number of instances.

MI measures the average uncertainty of information, nonnegativity. The range of *MI* is [0, 1] and a larger value means that the clustering results match the actual situation, which is calculated by Equation (8) [46].

$$MI(U, V) = \sum_{i=1}^{R} \sum_{j=1}^{C} P_{i,j} \log \left(\frac{P_{i,j}}{P_i \times P_j} \right) \tag{8}$$

where *R* is the number of categories of the prediction tag *U*, *C* is the category number of the real label *V*, P_i is the proportion of the number of *i-th* type data to the total data, and P_j is the proportion of the number of *j-th* type data to the number of total data.

2.4. Prediction Methods of TPIN

According to the verification of the feather selection method for machine-learning-based prediction [47], the mean decrease impurity (MDI) [48] was used to reduce the number of indicators used for prediction. Random forest (RF), gradient-boosted decision tree (GBDT), and SVM (poly) models were used for this study. Coefficient of determination

(R^2), mean square error (*MSE*), and mean absolute percentage error (*MAPE*) were used to evaluate the prediction effects. The calculation methods are shown in Equations (9)–(11).

$$R^2 = 1 - \frac{\sum_{i=1}^{n}\left(Y_i - \hat{Y}_i\right)^2}{\sum_{i=1}^{n}\left(Y_i - \overline{Y}_i\right)^2} \tag{9}$$

$$RMSE = \sqrt{\frac{1}{n}\sum_{i=1}^{n}\left(Y_i - \hat{Y}_i\right)^2} \tag{10}$$

$$MAPE = \frac{100\%}{n}\sum_{i=1}^{n}\left|\frac{Y_i - \hat{Y}_i}{Y_i}\right| \tag{11}$$

where Y_i is the actual value of TPIN, n is the sample size of Y_i, $\hat{Y}_i$ is the prediction value of TPIN, and Y_i is the mean of the actual TPIN values.

3. Results and Discussion

3.1. Section Selection Based on TPIN and Pavement Performance Detection Data

The box pattern based on the speed interval is drawn to analyze the influence of the instantaneous speed on TPIN (2393 samples), as shown in Figure 4, the points of the triangle represent abnormal deviations based on the statistical characteristics of the pavement texture conforming to a normal distribution.
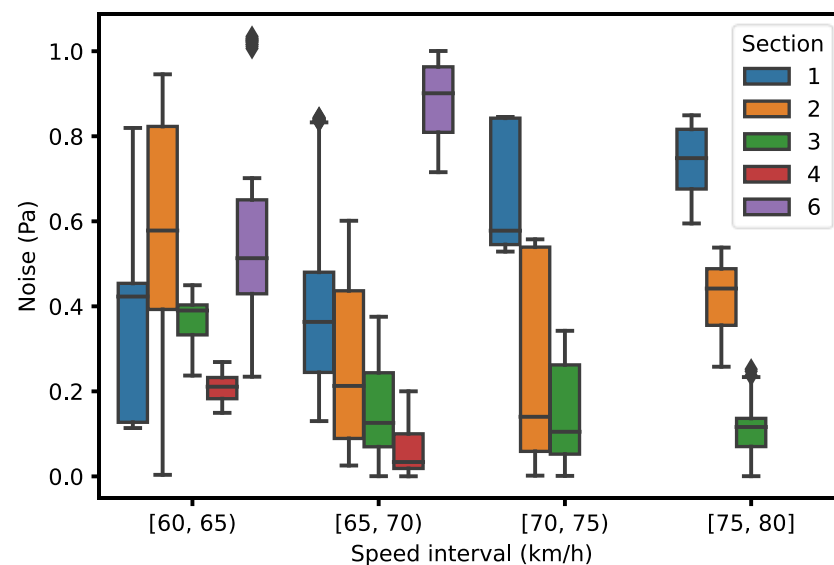

Figure 4. Distribution box plot of TPIN data.

As can be seen from Figure 4, when the speed reaches 65 km/h or above, the TPIN test results are relatively stable, and the higher the speed, the stronger the differentiation. Pavement Sections 1–3 with enough data were chosen for further study, and TPIN data at speeds of 75~80 km/h were selected as the prediction goals.

The correlations of IRI, MPD, and TPIN data are shown in Figure 5.

Figure 5 shows that IRI has almost no effect when the speed reaches about 80 km/h, and MPD has a certain influence. For the test results at the speed of 70 km/h, the influence of IRI increases slightly, but the influences of both MPD and IRI are weak. The statistically insignificant impact of IRI has also been proved by a multilevel Bayesian analysis of full-scale track testing data [25]. The results show that the influence of macroscopic indicators on TPIN can be ignored for the selected wear sections, and the analysis can be concentrated on texture metrics.
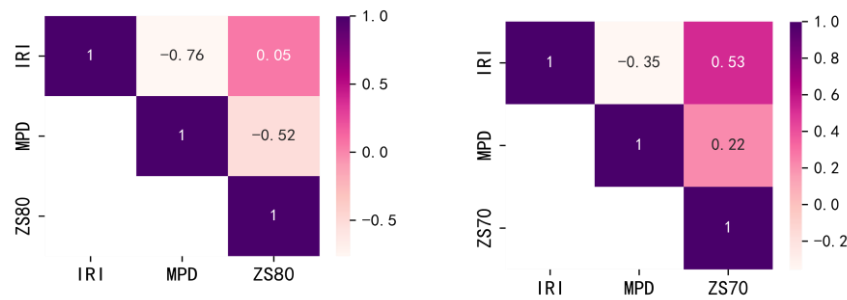
Figure 5. The correlations of IRI, MPD, and TPIN. (**Left**): ZS80 represents TPIN at 80 km/h. (**Right**): ZS70 represents TPIN at 70 km/h.

3.2. Spearman Correlation Analysis Results of Texture Metrics

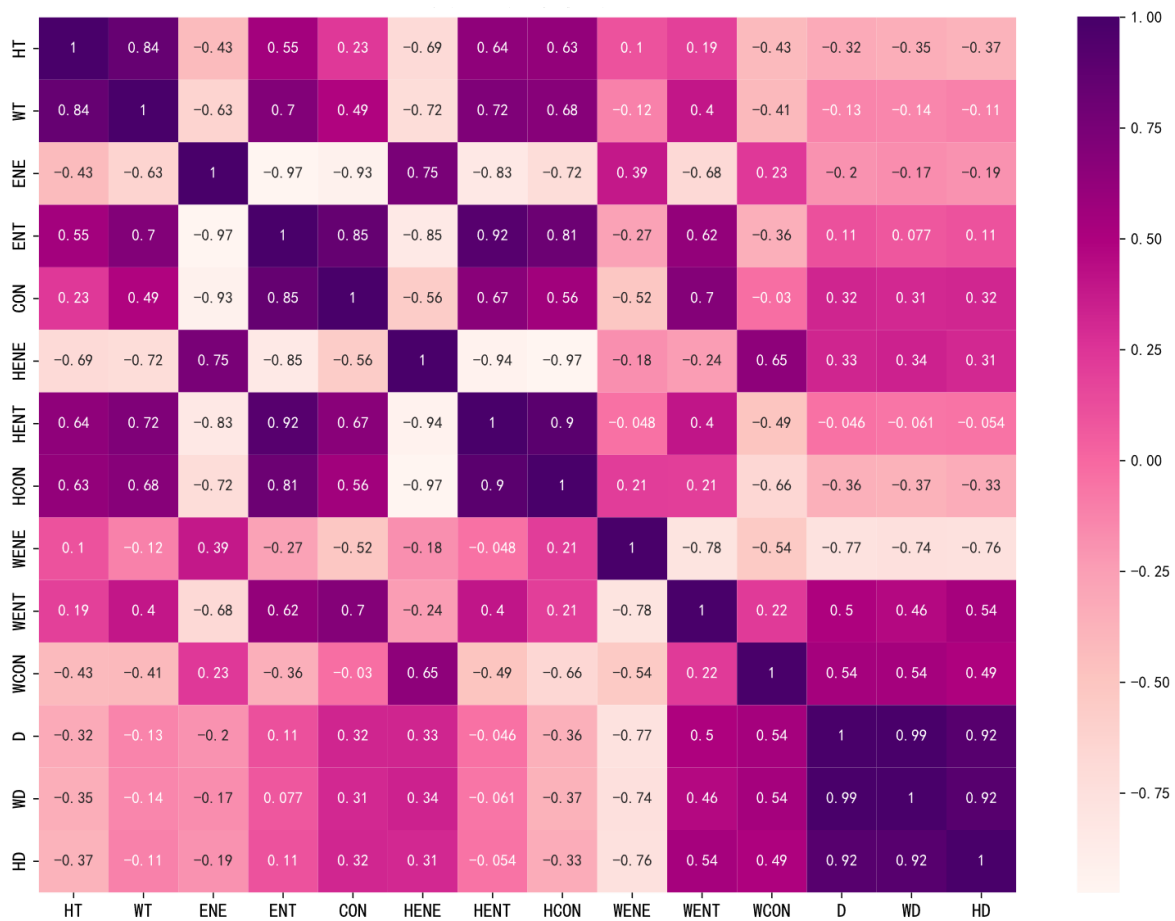The Spearman correlation coefficient results are shown in Figure 6.

Figure 6. Spearman correlation results.

It can be seen from Figure 6 that the correlation between the PSD indicators of macro-texture and microtexture is high (0.84). Since the PSD calculation requires selecting the frequency domain range, both HD and WD are retained for subsequent studies. Under the grey level co-occurrence matrix (GLCM) index system, the correlation between ENT and HENT reaches 0.99, the correlation between ENE and ENT reaches 0.96, the correlation between HENE and HCON reaches −0.98, the correlation between CON and ENE reaches −0.91, and the correlation between HCON and HENE reaches −0.98. Under the fractal dimension index system, the correlation between the total fractal dimension and the fractal

dimension that distinguishes macrotexture and microtexture is very high, so only the fractal dimension (D) was chosen to represent this index system among these three.

Above all, there are a large number of redundant metrics. According to the correlation magnitude between the metrics and the actual physical meaning of these metrics, HT, WT, CON, HENT, WENT, and D were selected for the follow-up study.

3.3. Clustering Results

3.3.1. The Internal Clustering Evaluation Results

The internal evaluation results of clustering are shown in Table 1.

Table 1. Flustering model evaluation based on the internal metrics.

Data	K	CH	DBI	SC
Field and Lab	2	363.3304	0.4447	0.82252
	3	372.1617	0.5443	0.6967
	4	483.8602	0.4473	0.7765
Field	2	350.8164	0.3385	0.8969
	3	335.7978	0.4866	0.8220
	4	476.5886	0.5122	0.8076
Lab	2	68.6601	0.5620	0.6977
	3	184.5086	0.3553	0.8225
	4	196.5702	0.5417	0.7037
	5	300.9437	0.4385	0.7904

As seen in Table 1, the SC clustering scores were high overall, and the CH index showed that the clustering results of field data were generally better than those of lab tests. This is due to the relatively high variability of the data from the smaller amount of specimens.

For field data, classification into two categories shows the best results, but the actual class number is three. This may be due to the discontinuity of the data, two types of pavement textures closer to each other, and another type more different from them. For laboratory data, classification into three categories is the best. The CH values for the laboratory data are positively correlated with the number of categories and are not informative. In the case of mixed field and lab test data, classification into four categories performs best, implying that the field and laboratory categories are well matched.

3.3.2. The External Clustering Evaluation Results

Based on the TPIN levels of the road, the pavements were divided into three categories, and the specimens were divided into four categories based on the specimen type and load conditions.

The classification and clustering results are shown in Appendix A (Tables A1–A3). The external evaluation results of clustering are shown in Table 2.

Table 2. External evaluation results of clustering analysis.

Data	K	RI	MI	Purity
Field and Lab	2	0.6125	0.4870	0.4059
	3	0.6715	0.4788	0.3762
	4	0.7366	0.6250	0.4653
Field	2	0.7332	0.4712	0.6507
	3	0.7639	0.5324	0.7460
	4	0.7363	0.5534	0.7460
Lab	2	0.5348	0.2802	0.4474
	3	0.6984	0.5520	0.5263
	4	0.7311	0.6209	0.5526
	5	0.7340	0.7492	0.5789

As can be seen in Table 2, the overall external evaluation results are generally consistent with the internal evaluation indicators. The classification effect of the laboratory data is worse compared to field data, partly because the sample of laboratory data is small and partly because the classification of laboratory data based on loading conditions has certain shortcomings. The field data still showed the best results for the three classes, consistent with the internal evaluation results. SVM classification of six uniformly nonporous asphalt pavements with different macrotextures using TPIN data demonstrates the method's feasibility from another perspective [10]. For $K = 4$, the laboratory data could match the actual pavement data best.

3.3.3. The Clustering Results Analysis

The clustering results and the metrics involved for field and lab data are shown in Figures 7–9. The Arabic data in the legend correspond to the K values of clustering, and the hollow symbols correspond to the artificially specified objective classification.
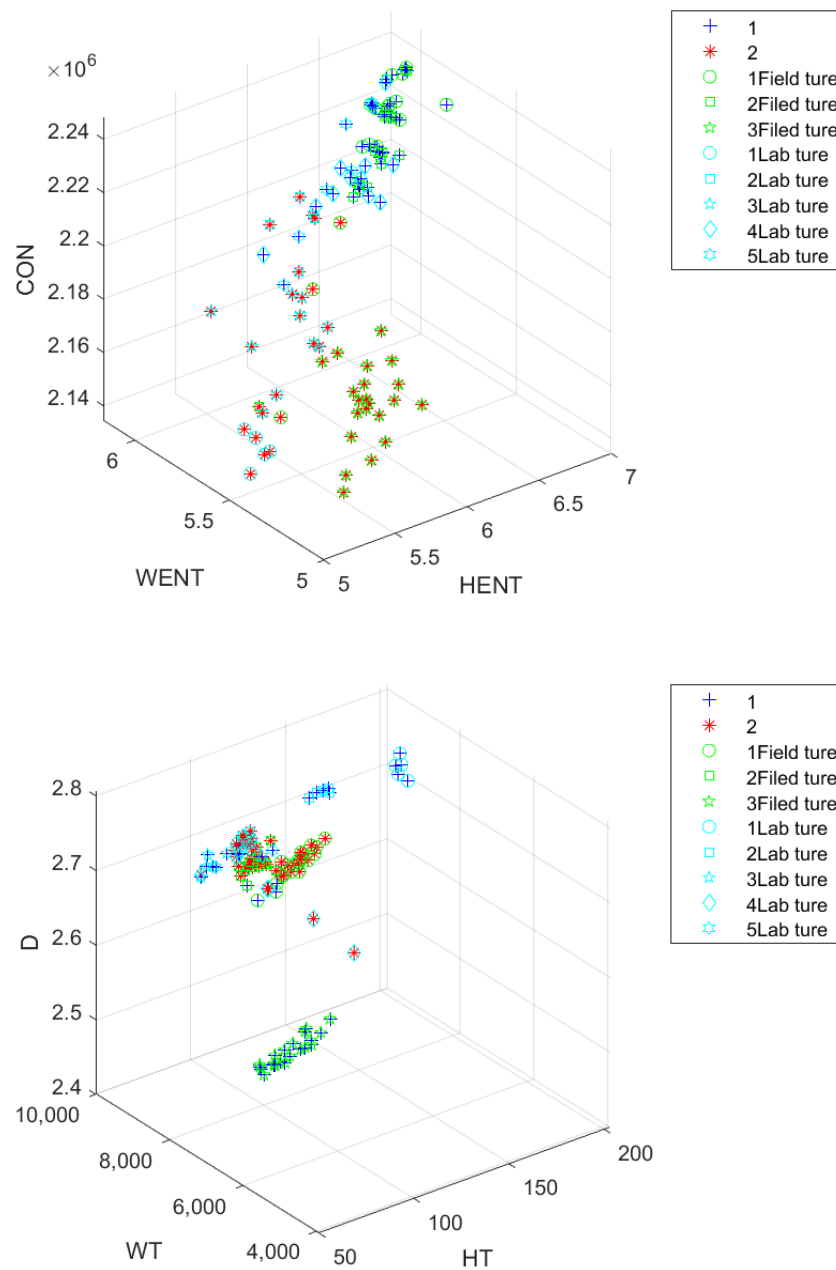

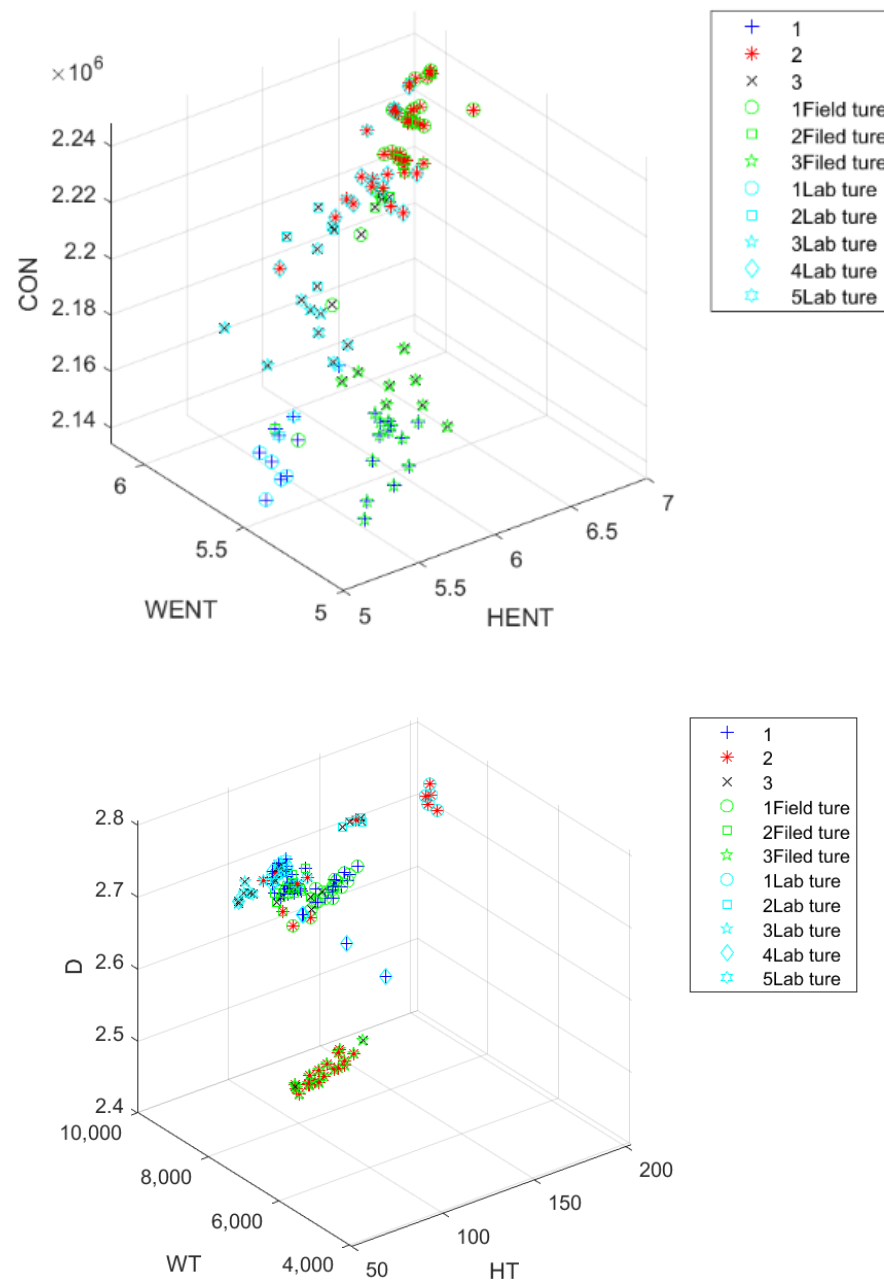**Figure 7.** Clustering results (two classes).

Figure 8. Clustering results (three classes).

As seen in Figure 7, the attempt to distinguish between the two types of divisions does not work well. There is a mixed grouping of lab and field test results. This is mainly due to the effect produced by abrasion, making the specimens similar to the actual pavement.

Figure 8 shows that the actual pavements match well with the clustering results. However, the texture metrics of the roads are not continuous; Sections 1 and 2 are similar, and Section 3 is more differentiated from Sections 1 and 2. The lab classification of three categories is better than the two categories. This may be due to the inability of the two classification categories to match the specimen's interval of texture characteristics.

Figure 9 shows that the clustering based on the four categories has an additional category of data with a low match to the actual road, representing a situation where the actual test road failed to match certain laboratory test specimens.

Comparing the metrics used (Figures 7–9), we find that the clustering results are almost chaotic regarding the distribution of *HT* values; *D* and *WT* perform better. Effective complementarity can be achieved among GLCM metrics.
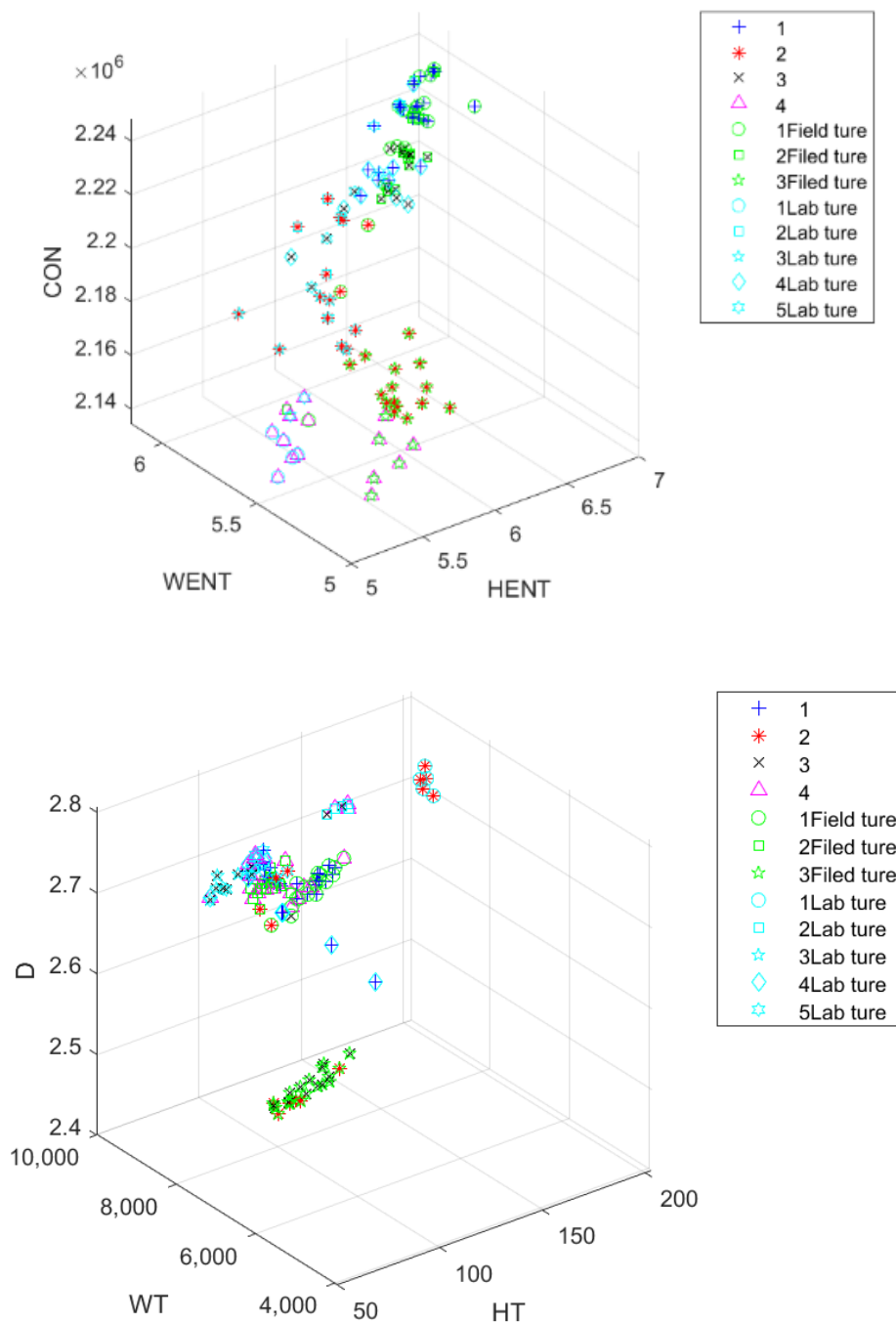

Figure 9. Clustering results (four classes).

3.4. TPIN Prediction Results

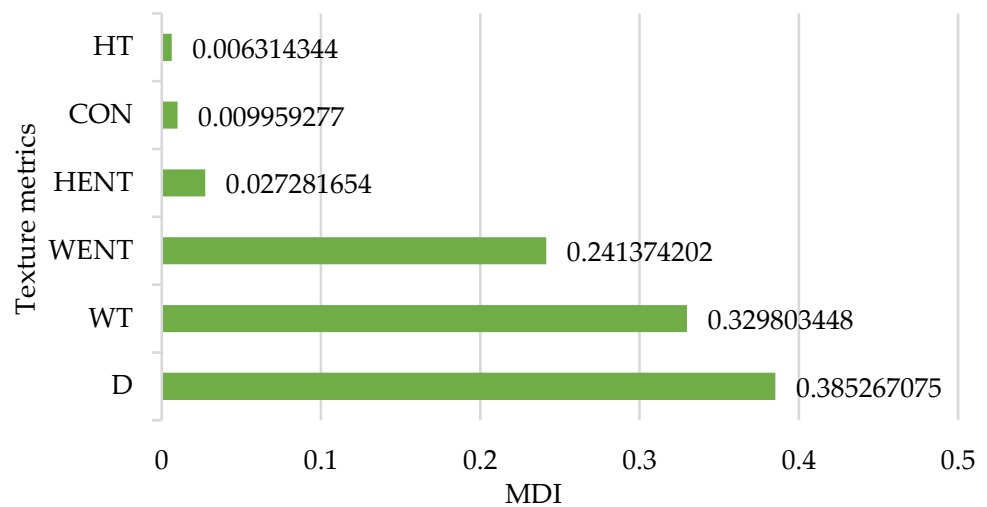The MDIs are sorted and shown in Figure 10.

Figure 10. The MDIs of the six indicators.

As seen in Figure 10, the top three indicators are *D, WT,* and *WENT*, which are consistent with the numerical concentration of indicators for the same road sections, implying that these metrics are statistically representative. The three metrics (*D, WT,* and *WENT*) were selected for subsequent prediction. Machine learning models, including RF, GBDT, and SVM methods, were used to predict TPIN at 80 km/h (training: test = 6:4). The prediction evaluation and the previous research results for comparison are also summarized and shown in Table 3.

Table 3. Accuracy evaluation of prediction models.

The Prediction Model	*MAPE*	*MSE*	R^2	Data Description
RF	0.0471	0.0009	0.9797	
GBDT	0.0376	0.0002	0.9958	Field test data of sound pressure
SVM	0.0824	0.0072	0.8688	
F-test results of linear model [13]	/	/	0.94	Lab test, low speed (23.9 km/h)
Bayesian multilevel model [24]	/	/	0.968	Field test data of sound pressure

As seen in Table 3, the accuracies of GBDT and RF models are acceptable, and GBDT performs best. The prediction and error plots of GBDT and RF models are shown in Figures 11 and 12.

As can be seen from Figures 11 and 12, the TPIN prediction accuracies are high, and the errors are relatively low, which meets the requirements of the TPIN level assessment. In terms of noise distribution, the higher the TPIN value, the higher the error.
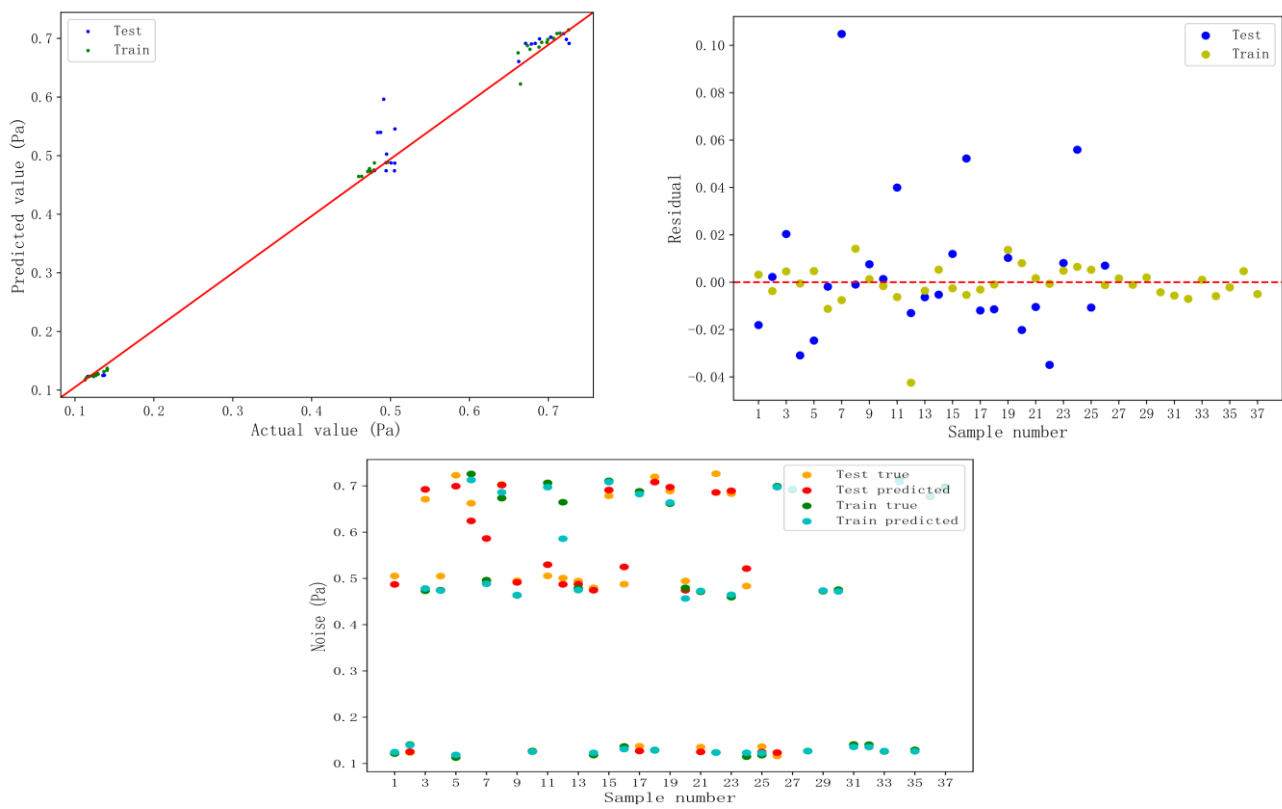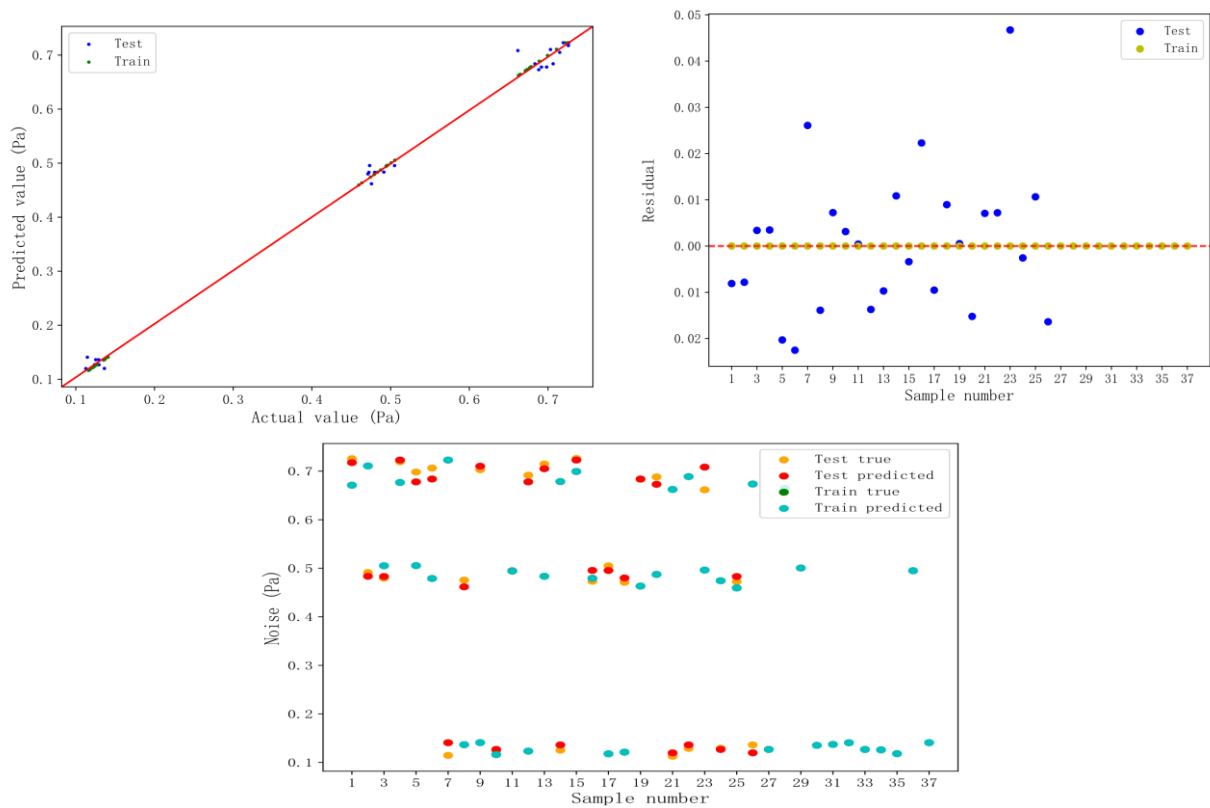
Figure 11. RF prediction results.

Figure 12. GBDT prediction results.

4. Conclusions

This study used a close-range 3D camera to obtain the point cloud data. The representative 3D texture metrics were selected based on Spearman correlation analysis. Texture data from lab and field were mixed to conduct a clustering analysis to determine the feasibility of using a combination of texture metrics for TPIN level classification. Finally, TPIN prediction models based on texture metrics selected were established and evaluated.

The contributions of this paper are as follows:

1. A method including preprocessing of 3D cloud data, pavement texture clustering, and TPIN prediction based on machine learning is proposed to predict TPIN.
2. Macro- and microtexture statistics metrics are feasible for wear lab and field universal study, and the metrics combined can be used to sort different wear and TPIN levels.
3. The GBDT prediction model with *D*, *WT*, and *WENT* reaches a high accuracy ($R^2 = 0.9958$, $MSE = 0.0002$).

As the number of data is small and the types of mixtures are limited, different mixes or pavement types should be further investigated based on more data. In addition, different road conditions may have different requirements for data processing, such as interference with data from larger deformations.

Appendix A

Table A1. Field texture, TPIN data, and clustering results.

Section	Class	*HT*	*WT*	*CON*	*HENT*	*WENT*	*D*	*K* = 2	*K* = 3	*K* = 4	N80
1	1	140.2518	9737.459	2,190,876	6.365243	5.948285	2.606582	2	3	1	0.6617
1	1	140.5601	9769.212	2,170,543	6.16111	5.935611	2.59399	2	1	2	0.6625
1	1	157.0259	9914.391	2,227,109	6.670939	5.864591	2.61801	1	2	3	0.6712
1	1	130.5765	9755.94	2,140,465	5.688288	5.747524	2.592336	2	1	4	0.6646
1	1	154.7143	9895.534	2,228,456	6.62285	5.983071	2.615811	1	2	3	0.6735
1	1	170.6463	9997.196	2,215,659	6.59751	5.930476	2.630418	1	3	1	0.6767
1	1	160.6162	9928.916	2,225,385	6.678157	5.926658	2.613039	1	2	3	0.6786
1	1	164.9753	9929.28	2,228,794	6.709074	5.944194	2.626497	1	2	3	0.6834
1	1	162.6561	9961.723	2,236,390	6.809056	5.723936	2.629737	1	2	3	0.6882
1	1	157.0566	9882.437	2,227,350	6.778483	5.965392	2.626263	1	2	3	0.6889
1	1	164.066	9922.555	2,240,394	6.815592	5.940327	2.618399	1	2	3	0.6982
1	1	154.3935	9856.267	2,237,931	6.745962	5.964423	2.605496	1	2	3	0.6994
1	1	164.066	9922.555	2,240,394	6.815592	5.940327	2.618399	1	2	3	0.6916

Table A1. *Cont.*

Section	Class	HT	WT	CON	HENT	WENT	D	K = 2	K = 3	K = 4	N80
1	1	156.2884	9897.427	2,227,388	6.637929	5.971619	2.628652	1	2	3	0.7065
1	1	144.0166	9809.265	2,227,559	6.706778	5.95351	2.610949	1	2	3	0.7031
1	1	149.3278	9803.716	2,226,865	6.648029	5.974447	2.611791	1	2	3	0.7108
1	1	144.1535	9764.203	2,215,347	6.537224	5.960762	2.612284	1	3	1	0.7148
1	1	153.7648	9821.965	2,227,550	6.704577	5.952067	2.623179	1	2	3	0.7229
1	1	147.1195	9787.418	2,202,573	6.502314	5.959001	2.622824	1	3	1	0.7258
1	1	151.1389	9825.045	2,215,502	6.580022	5.957422	2.618354	1	3	1	0.7194
1	1	142.8201	9738.662	2,237,826	6.803949	5.951798	2.633391	1	2	3	0.7263
2	2	120.306	9496.202	2,141,056	5.652265	5.836816	2.629105	2	1	4	0.4795
2	2	123.4363	9423.833	2,225,290	6.705251	5.909514	2.66954	1	2	3	0.479
2	2	116.6561	9383.842	2,213,950	6.529906	5.855884	2.656537	1	3	1	0.4733
2	2	125.6373	9429.803	2,227,682	6.631201	5.915074	2.659555	1	2	3	0.4711
2	2	124.2467	9436.715	2,239,266	6.823183	5.940351	2.678627	1	2	3	0.4634
2	2	124.8888	9484.089	2,239,803	6.802336	5.938466	2.664685	1	2	3	0.4757
2	2	114.8213	9401.472	2,202,477	6.388935	5.893785	2.650193	1	3	1	0.4724
2	2	120.5244	9417.797	2,238,557	6.680337	5.941778	2.66832	1	2	3	0.4596
2	2	126.7114	9549.294	2,225,932	6.650289	5.929108	2.657626	1	2	3	0.4744
2	2	126.2311	9498.468	2,215,604	6.571671	5.899318	2.650512	1	3	1	0.4797
2	2	136.9934	9592.793	2,202,028	6.499463	5.952634	2.631535	1	3	1	0.4914
2	2	130.6252	9542.905	2,225,081	6.694389	5.927791	2.649595	1	2	3	0.4874
2	2	131.6491	9576.468	2,226,275	6.685228	5.944888	2.645004	1	2	3	0.4835
2	2	128.2213	9510.897	2,215,332	6.586884	5.930047	2.652833	1	3	1	0.495
2	2	120.996	9395.484	2,213,502	6.621387	5.916992	2.655977	1	3	1	0.4944
2	2	118.0208	9374.048	2,215,721	6.576274	5.885727	2.660711	1	3	1	0.4963
2	2	116.7086	9373.504	2,202,736	6.46337	5.916607	2.656968	1	3	1	0.4943
2	2	118.1459	9336.264	2,213,803	6.566077	5.890992	2.667591	1	3	1	0.5006
2	2	121.5127	9397.591	2,203,390	6.499117	5.904437	2.663514	1	3	1	0.505
2	2	111.4096	9294.882	2,215,074	6.571895	5.920085	2.669541	1	3	1	0.5053
2	2	133.3873	9535.165	2,213,571	6.673446	5.870046	2.675986	1	3	1	0.5055
3	3	118.8022	8190.827	2,170,419	5.838518	5.118374	2.459816	2	1	2	0.1363
3	3	138.5395	8193.125	2,181,998	5.958741	5.42493	2.47402	2	1	2	0.1408
3	3	126.7313	8230.696	2,162,734	5.890374	5.301612	2.471123	2	1	2	0.1409
3	3	103.3065	7897.602	2,162,401	5.715989	5.316755	2.453879	2	1	2	0.1373
3	3	110.7464	8109.603	2,145,140	5.700261	5.280097	2.444492	2	1	4	0.1407
3	3	109.8774	7937.153	2,153,412	5.622871	5.326607	2.449603	2	1	4	0.1367
3	3	124.7071	8001.231	2,170,730	5.863384	5.426774	2.463782	2	1	2	0.1294
3	3	120.4148	7935.903	2,162,511	5.773219	5.429787	2.46034	2	1	2	0.1353
3	3	93.96805	7802.107	2,180,690	5.824387	5.265382	2.463394	2	1	2	0.127
3	3	94.80948	7806.527	2,166,863	5.658132	5.314213	2.459358	2	1	2	0.129
3	3	99.93752	7732.5	2,171,267	5.716613	5.328969	2.463718	2	1	2	0.1253
3	3	102.6348	7834.169	2,138,417	5.480241	5.259559	2.456323	2	1	4	0.1234
3	3	99.65145	7693.064	2,161,535	5.742149	5.268382	2.477157	2	1	2	0.1238
3	3	114.0515	8022.764	2,162,486	5.759748	5.337354	2.451916	2	1	2	0.1269
3	3	133.6847	8192.826	2,153,492	5.814196	5.43795	2.460119	2	1	4	0.126
3	3	99.31789	7972.859	2,153,083	5.743936	5.239729	2.442288	2	1	4	0.1213
3	3	96.88123	7957.785	2,144,846	5.490411	5.253704	2.458167	2	1	4	0.1179
3	3	123.9664	8130.17	2,170,655	5.874836	5.267573	2.472092	2	1	2	0.1181
3	3	127.7747	8133.874	2,162,651	5.777118	5.365302	2.450702	2	1	2	0.1147
3	3	118.9286	7976.812	2,171,025	5.689691	5.532551	2.457837	2	1	2	0.1163
3	3	109.5175	7934.195	2,172,858	5.78724	5.521902	2.467659	2	1	2	0.1127

Table A2. Clustering results for lab data.

Temperature (°C)	Load (kg)	Grid Time (h)	Mix Type	Class	HT	WT	CON	HENT	WENT	D	K = 2	K = 3	K = 4	K = 5
25	100	1	EA10	4	200.1252	9474.22	2,142,466	5.398496	5.661241	2.733111	2	2	3	2
25	100	2	EA10	4	197.8918	9478.957	2,143,549	5.387827	5.710816	2.718602	2	2	3	2
25	100	3	EA10	4	202.5992	9550.427	2,137,786	5.453854	5.628504	2.713419	2	2	3	2
25	100	4	EA10	4	200.4735	9532.335	2,143,087	5.312544	5.547858	2.702988	2	2	3	2
25	100	1	EA10	4	203.5031	9428.059	2,134,256	5.277661	5.598742	2.694699	2	2	3	2
25	100	3	AC10	5	134.4078	8160.089	2,171,093	6.211048	6.047009	2.785007	2	1	4	1
25	100	1	AC10	5	117.052	7656.542	2,186,354	6.126969	6.135854	2.806571	1	1	2	1
25	100	1	AC10	5	125.8476	7895.707	2,190,935	6.371675	6.162665	2.798043	1	1	2	1
25	100	2	AC10	5	139.006	8244.898	2,192,201	6.276161	6.023843	2.775359	1	1	2	1
25	100	4	AC10	5	137.244	8165.502	2,191,308	6.277131	6.015132	2.784678	1	1	2	1
25	50	1	SMA10	6	61.96747	7761.138	2,183,390	5.259744	5.576053	2.748872	1	1	2	1
25	75	1	SMA10	6	80.415	8002.265	2,165,689	5.873896	5.68852	2.756023	2	2	4	1
25	50	2	SMA10	6	65.62519	7783.155	2,186,631	5.268074	5.795175	2.758699	1	1	2	1
25	50	3	SMA10	6	66.72891	7817.642	2,188,823	5.698766	5.696648	2.772231	1	1	2	1
25	75	2	SMA10	6	89.77065	8134.768	2,188,164	5.731191	5.666633	2.742637	1	1	2	1
25	100	1	SMA10	7	68.5346	3916.921	2,226,383	5.874341	5.615758	2.758084	1	3	1	5
25	150	1	SMA10	7	99.11652	8313.325	2,238,468	6.441615	5.832935	2.743714	1	3	1	5
25	50	4	SMA10	7	64.39665	7883.11	2,205,752	5.53187	5.723417	2.746018	1	1	2	4
25	100	2	SMA10	7	73.08235	5278.396	2,231,365	5.970311	5.596111	2.75817	1	3	1	5
25	75	3	SMA10	7	90.20172	8237.601	2,215,546	6.220091	5.689277	2.752201	1	3	1	4
25	75	4	SMA10	7	90.27892	8238.604	2,230,901	6.258402	5.585971	2.734297	1	3	1	5
25	100	3	SMA10	7	74.12594	6561.373	2,229,072	6.0399	5.699512	2.757991	1	3	1	5
25	150	2	SMA10	7	92.34798	8239.015	2,248,238	6.473895	5.791404	2.748601	1	3	1	3
25	100	4	SMA10	7	74.5372	6560.45	2,229,131	6.054549	5.602095	2.75715	1	3	1	5
10	100	1	SMA10	7	85.94515	7801.888	2,207,245	6.066941	5.84916	2.776292	1	1	2	4
40	100	1	SMA10	7	102.0044	8446.173	2,215,685	6.226914	5.630642	2.74203	1	3	1	4
40	100	2	SMA10	7	103.6456	8540.191	2,232,364	6.10359	5.619615	2.722978	1	3	1	5
25	150	3	SMA10	8	97.4696	8329.697	2,239,223	6.441555	5.839455	2.74283	1	3	1	5
25	150	4	SMA10	8	90.91534	8315.082	2,232,870	6.297493	5.864532	2.74015	1	3	1	5
10	100	2	SMA10	8	84.76578	7781.25	2,198,559	5.950772	5.850172	2.777894	1	1	2	4
60	100	1	SMA10	8	91.1343	8198.318	2,174,016	5.724007	5.598527	2.749057	2	1	4	1
10	100	3	SMA10	8	84.99197	7802.974	2,212,197	6.142412	5.848673	2.781691	1	3	1	4
40	100	3	SMA10	8	114.7557	8531.808	2,144,505	5.563857	5.749093	2.710942	2	2	3	2
10	100	4	SMA10	8	89.43663	7839.255	2,223,554	6.173675	5.741891	2.78192	1	3	1	5
40	100	4	SMA10	8	112.0517	8666.278	2,149,006	5.667467	5.753685	2.701373	2	2	3	2
60	100	2	SMA10	8	90.15488	8182.348	2,194,519	5.619295	5.679922	2.738758	1	1	2	1
60	100	3	SMA10	8	77.39062	8219.836	2,179,930	5.749463	5.691116	2.734488	2	1	4	1
60	100	4	SMA10	8	79.05924	8229.404	2,183,417	5.724156	5.529839	2.73144	1	1	2	1

Table A3. Clustering results for lab and field data.

Sample Number	Items	Class	K = 2	K = 3	K = 4
1	1	1	2	3	3
2	1	1	1	1	4
3	1	1	1	2	4
4	1	1	1	2	4
5	1	1	1	2	4
6	1	1	1	2	2
7	1	1	1	2	2
8	1	1	1	2	2
9	1	1	1	2	2
10	1	1	1	2	2
11	1	1	1	2	2
12	1	1	1	2	2
13	1	1	1	2	2
14	1	1	1	2	2
15	1	1	1	2	2
16	1	1	1	2	2
17	1	1	1	2	2
18	1	1	1	2	2
19	1	1	1	2	2
20	1	1	2	1	1
21	1	1	2	1	1
22	2	2	2	3	3
23	2	2	1	2	4
24	2	2	1	1	4
25	2	2	1	2	4
26	2	2	1	2	4
27	2	2	1	2	4
28	2	2	1	1	4
29	2	2	1	2	4
30	2	2	1	2	4
31	2	2	1	1	4
32	2	2	1	2	4
33	2	2	1	1	4
34	2	2	1	2	4
35	2	2	1	2	2
36	2	2	1	2	2
37	2	2	1	2	2
38	2	2	1	2	2
39	2	2	1	2	2
40	2	2	1	2	2
41	2	2	1	2	2
42	2	2	1	2	2
43	3	3	2	3	1
44	3	3	2	3	3
45	3	3	2	3	3
46	3	3	2	3	3
47	3	3	2	3	1
48	3	3	2	3	1
49	3	3	2	3	3
50	3	3	2	3	1
51	3	3	2	3	3
52	3	3	2	3	3
53	3	3	2	3	1
54	3	3	2	3	1
55	3	3	2	1	1
56	3	3	2	1	1
57	3	3	2	1	1
58	3	3	2	1	1

Table A3. *Cont.*

Sample Number	Items	Class	K = 2	K = 3	K = 4
59	3	3	2	3	1
60	3	3	2	1	1
61	3	3	2	1	1
62	3	3	2	1	1
63	3	3	2	1	1
64	EA10	4	2	3	3
65	EA10	4	2	3	3
66	EA10	4	2	3	3
67	EA10	4	2	3	3
68	EA10	4	2	3	3
69	AC10	5	2	1	1
70	AC10	5	2	1	1
71	AC10	5	2	1	1
72	AC10	5	2	1	1
73	AC10	5	2	1	1
74	SMA10	6	2	1	1
75	SMA10	6	2	3	1
76	SMA10	6	2	1	1
77	SMA10	6	2	1	1
78	SMA10	6	2	1	1
79	SMA10	7	1	2	2
80	SMA10	7	1	2	2
81	SMA10	7	1	1	4
82	SMA10	7	1	2	2
83	SMA10	7	1	2	4
84	SMA10	7	1	2	2
85	SMA10	7	1	2	2
86	SMA10	7	1	2	2
87	SMA10	7	1	2	2
88	SMA10	7	1	2	4
89	SMA10	7	1	2	4
90	SMA10	7	1	2	2
91	SMA10	8	1	2	2
92	SMA10	8	1	2	2
93	SMA10	8	1	1	4
94	SMA10	8	2	1	1
95	SMA10	8	1	2	4
96	SMA10	8	2	3	3
97	SMA10	8	1	2	2
98	SMA10	8	2	3	3
99	SMA10	8	1	1	4
100	SMA10	8	2	1	1
101	SMA10	8	2	1	1

References

1. Li, Q.; Qiao, F.; Lei, Y. Impacts of pavement types on in-vehicle noise and human health. *J. Air Waste Manag. Assoc.* **2016**, *66*, 87–96. [CrossRef] [PubMed]
2. Abu Dabous, S.; Zeiada, W.; Zayed, T.; Al-Ruzouq, R. Sustainability-informed multi-criteria decision support framework for ranking and prioritization of pavement sections. *J. Clean. Prod.* **2019**, *244*, 118755. [CrossRef]
3. Yang, W.; He, J.; He, C.; Cai, M. Evaluation of urban traffic noise pollution based on noise maps. *Transp. Res. Part D Transp. Environ.* **2020**, *87*, 102516. [CrossRef]
4. Khajehvand, M.; Rassafi, A.A.; Mirbaha, B. Modeling traffic noise level near at-grade junctions: Roundabouts, T and cross intersections. *Transp. Res. Part D Transp. Environ.* **2021**, *93*, 102752. [CrossRef]
5. Cao, R.; Leng, Z.; Yu, J.; Hsu, S.-C. Multi-objective optimization for maintaining low-noise pavement network system in Hong Kong. *Transp. Res. Part D Transp. Environ.* **2020**, *88*, 102573. [CrossRef]
6. Nowoświat, A.; Sorociak, W.; Żuchowski, R. The impact of the application of thin emulsion mat microsurfacing on the level of noise in the environment. *Constr. Build. Mater.* **2020**, *263*, 120626. [CrossRef]

7. Bernhard, R.; Wayson, R.L.; Haddock, J.; Neithalath, N.; El-Aassar, A.; Olek, J.; Pellinen, T.; Weiss, W.J. *An Introduction to Tire/Pavement Noise of Asphalt Pavement*; Institute of Safe, Quiet and Durable Highways, Purdue University: West Lafayette, IN, USA, 2005.
8. Staiano, M.A. Tire–Pavement Noise and Pavement Texture. *J. Transp. Eng. Part B Pavements* **2018**, *144*, 04018034. [CrossRef]
9. Ganji, M.R.; Golroo, A.; Sheikhzadeh, H.; Ghelmani, A.; Bidgoli, M.A. Dense-graded asphalt pavement macrotexture measurement using tire/road noise monitoring. *Autom. Constr.* **2019**, *106*, 102887. [CrossRef]
10. Ganji, M.R.; Ghelmani, A.; Golroo, A.; Sheikhzadeh, H. Mean texture depth measurement with an acoustical-based apparatus using cepstral signal processing and support vector machine. *Appl. Acoust.* **2019**, *161*, 107168. [CrossRef]
11. Mikhailenko, P.; Piao, Z.; Kakar, M.R.; Bueno, M.; Athari, S.; Pieren, R.; Heutschi, K.; Poulikakos, L. Low-Noise pavement technologies and evaluation techniques: A literature review. *Int. J. Pavement Eng.* **2020**, *23*, 1911–1934. [CrossRef]
12. Chen, D.; Han, S.; Ren, X.; Ye, A.; Wang, W.; Su, Q.; Wang, T. Measuring the tyre/pavement noise using laboratory tyre rolling-down method. *Int. J. Pavement Eng.* **2019**, *21*, 1595–1605. [CrossRef]
13. Han, S.; Peng, B.; Chu, L.; Fwa, T.F. In-door laboratory high-speed testing of tire-pavement noise. *Int. J. Pavement Eng.* **2020**, *23*, 321–331. [CrossRef]
14. Li, T. A Review on Physical Mechanisms of Tire-Pavement Interaction Noise. *SAE Int. J. Veh. Dyn. Stab. NVH* **2019**, *3*, 87–112. [CrossRef]
15. Chen, D.; Ling, C.; Wang, T.; Su, Q.; Ye, A. Prediction of tire-pavement noise of porous asphalt mixture based on mixture surface texture level and distributions. *Constr. Build. Mater.* **2018**, *173*, 801–810. [CrossRef]
16. Zhang, H.; Liu, Z.; Meng, X. Noise reduction characteristics of asphalt pavement based on indoor simulation tests. *Constr. Build. Mater.* **2019**, *215*, 285–297. [CrossRef]
17. Praticò, F.G.; Fedele, R.; Pellicano, G. Pavement FRFs and noise: A theoretical and experimental investigation. *Constr. Build. Mater.* **2021**, *294*, 123487. [CrossRef]
18. Chen, J.; Yin, X.; Wang, H.; Ding, Y. Evaluation of durability and functional performance of porous polyurethane mixture in porous pavement. *J. Clean. Prod.* **2018**, *188*, 12–19. [CrossRef]
19. Šernas, O.; Vaitkus, A.; Gražulytė, J.; Skrodenis, D.; Wasilewska, M.; Gierasimiuk, P. Development of low noise and durable semi-dense asphalt mixtures. *Constr. Build. Mater.* **2021**, *293*, 123413. [CrossRef]
20. Vázquez, V.; Terán, F.; Huertas, P.; Paje, S. Field assessment of a Cold-In place-recycled pavement: Influence on rolling noise. *J. Clean. Prod.* **2018**, *197*, 154–162. [CrossRef]
21. Dong, S.; Han, S.; Yin, Y.; Zhang, Z.; Yao, T. The method for accurate acquisition of pavement macro-texture and corresponding finite element model based on three-dimensional point cloud data. *Constr. Build. Mater.* **2021**, *312*, 125390. [CrossRef]
22. Lou, K.; Xiao, P.; Kang, A.; Wu, Z.; Dong, X. Effects of asphalt pavement characteristics on traffic noise reduction in different frequencies. *Transp. Res. Part D Transp. Environ.* **2022**, *106*, 103259. [CrossRef]
23. Li, Y.; Qin, Y.; Wang, H.; Xu, S.; Li, S. Study of Texture Indicators Applied to Pavement Wear Analysis Based on 3D Image Technology. *Sensors* **2022**, *22*, 4955. [CrossRef] [PubMed]
24. Vázquez, V.F.; Terán, F.; Huertas, P.; Paje, S.E. Surface Aging Effect on Tire/Pavement Noise Medium-Term Evolution in a Medium-Size City. *Coatings* **2018**, *8*, 206. [CrossRef]
25. Chen, L.; Cong, L.; Dong, Y.; Yang, G.; Tang, B.; Wang, X.; Gong, H. Investigation of influential factors of tire/pavement noise: A multilevel Bayesian analysis of full-scale track testing data. *Constr. Build. Mater.* **2021**, *270*, 121484. [CrossRef]
26. Li, T. A state-of-the-art review of measurement techniques on tire–pavement interaction noise. *Measurement* **2018**, *128*, 325–351. [CrossRef]
27. Li, T. Influencing Parameters on Tire–Pavement Interaction Noise: Review, Experiments, and Design Considerations. *Designs* **2018**, *2*, 38. [CrossRef]
28. Bassil, M.B.L.; Cesbron, J.; Klein, P. Tyre/road noise: A piston approach for CFD modeling of air volume variation in a cylindrical road cavity. *J. Sound Vib.* **2019**, *469*, 115140. [CrossRef]
29. Ding, Y.; Wang, H. FEM-BEM analysis of tyre-pavement noise on porous asphalt surfaces with different textures. *Int. J. Pavement Eng.* **2017**, *20*, 1090–1097. [CrossRef]
30. Kleizienė, R.; Šernas, O.; Vaitkus, A.; Simanavičienė, R. Asphalt Pavement Acoustic Performance Model. *Sustainability* **2019**, *11*, 2938. [CrossRef]
31. Yang, W.; Cai, M.; Luo, P. The calculation of road traffic noise spectrum based on the noise spectral characteristics of single vehicles. *Appl. Acoust.* **2019**, *160*, 107128. [CrossRef]
32. Cao, R.; Leng, Z.; Hsu, S.-C.; Hung, W.-T. Modelling of the pavement acoustic longevity in Hong Kong through machine learning techniques. *Transp. Res. Part D Transp. Environ.* **2020**, *83*, 102366. [CrossRef]
33. Matlack, G.R.; Horn, A.; Aldo, A.; Walubita, L.F.; Naik, B.; Khoury, I. Measuring surface texture of in-service asphalt pavement: Evaluation of two proposed hand-portable methods. *Road Mater. Pavement Des.* **2021**, *2*, 1–17. [CrossRef]
34. Xin, Q.; Qian, Z.; Miao, Y.; Meng, L.; Wang, L. Three-dimensional characterisation of asphalt pavement macrotexture using laser scanner and micro element. *Road Mater. Pavement Des.* **2017**, *18*, 190–199. [CrossRef]
35. Chen, J.; Huang, X.; Zheng, B.; Zhao, R.; Liu, X.; Cao, Q.; Zhu, S. Real-time identification system of asphalt pavement texture based on the close-range photogrammetry. *Constr. Build. Mater.* **2019**, *226*, 910–919. [CrossRef]

36. Chen, D.; Sefidmazgi, N.R.; Bahia, H. Exploring the feasibility of evaluating asphalt pavement surface macro-texture using image-based texture analysis method. *Road Mater. Pavement Des.* **2014**, *16*, 405–420. [CrossRef]

37. Chen, D. Evaluating asphalt pavement surface texture using 3D digital imaging. *Int. J. Pavement Eng.* **2018**, *21*, 416–427. [CrossRef]

38. Dong, S.; Han, S.; Luo, Y.; Han, X.; Xu, O. Evaluation of tire-pavement noise based on three-dimensional pavement texture characteristics. *Constr. Build. Mater.* **2021**, *306*, 124935. [CrossRef]

39. Weng, Z.; Xiang, H.; Lin, Y.; Liu, C.; Wu, D.; Du, Y. Pavement texture depth estimation using image-based multiscale features. *Autom. Constr.* **2022**, *141*, 104404. [CrossRef]

40. Medeiros, M., Jr.; Babadopulos, L.; Maia, R.; Branco, V.C. 3D pavement macrotexture parameters from close range photogrammetry. *Int. J. Pavement Eng.* **2021**, 1–15. [CrossRef]

41. *Standard No. 13473-4*; Characterization of Pavement Texture by Use of Surface Profiles—Part 4: Spectral Analysis of Texture Profiles. ISO: Geneva, Switzerland.

42. Arthur, D.; Vassilvitskii, S. K-means++: The Advantages of Careful Seeding. In Proceedings of the SODA '07: Proceedings of the 18th Annual ACM-SIAM Symposium on Discrete Algorithms, New Orleans, LA, USA, 7–9 January 2007; pp. 1027–1035.

43. Pal, N.; Biswas, J. Cluster validation using graph theoretic concepts. *Pattern Recognit.* **1997**, *30*, 847–857. [CrossRef]

44. Nitya Sai, L.; Sai Shreya, M.; Anjan Subudhi, A.; Jaya Lakshmi, B.; Madhuri, K.B. Optimal K-Means Clustering Method Using Silhouette Coefficient. *Int. J. Appl. Res. Inf. Technol. Comput.* **2017**, *8*. [CrossRef]

45. Robert, V.; Vasseur, Y.; Brault, V. Comparing High-Dimensional Partitions with the Co-clustering Adjusted Rand Index. *J. Classif.* **2020**, *38*, 158–186. [CrossRef]

46. Hoang, T.; Do, T.-T.; Nguyen, T.V.; Cheung, N.-M. Multimodal Mutual Information Maximization: A Novel Approach for Unsupervised Deep Cross-Modal Hashing. *IEEE Trans. Neural Netw. Learn. Syst.* 2022, *in press*. [CrossRef] [PubMed]

47. Luo, Z.; Wang, H.; Li, S. Prediction of International Roughness Index Based on Stacking Fusion Model. *Sustainability* **2022**, *14*, 6949. [CrossRef]

48. Breiman, L. Manual on Setting Up, Using, and Understanding Random Forests v3.1. Technical Report. 2012. Available online: https://oz.berkeley.edu/users/breiman (accessed on 15 January 2022).